Construction and Building Materials 457 (2024) 139469

Contents lists available at ScienceDirect

Construction and Building Materials

journal homepage: www.elsevier.com/locate/conbuildmat

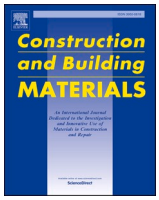

In-situ characterisation of early hydration of low-carbon cements containing thermally and mechanically activated kaolin

Jofre Mañosa [a], Manuel Torres-Carrasco [b], Javier C. Córdoba [a], Alex Maldonado-Alameda [c], Josep Maria Chimenos [a,*]

[a] Departament de Ciència de Materials i Química Física, Universitat de Barcelona, C/ Martí i Franquès 1, Barcelona 08028, Spain
[b] Materials Science and Engineering Department, IAAB, University Carlos III of Madrid, Avda. Universidad 30, Leganés 28911, Madrid, Spain
[c] Fundación Centro Tecnológico de Investigación Multisectorial (CETIM), Parque empresarial de Alvedro, Rúa H, 20, Culleredo 15180, A Coruña, Spain

ARTICLE INFO

Keywords:
LC^3
Clay activation
Calcined clay
Kaolinite
Early-age properties
Modified clay
Ternary blended cement

ABSTRACT

This study investigates the early hydration mechanism of limestone calcined clay cement (LC^3) system containing mechanically activated clay (MC) replacing thermally activated clay (calcined clay, CC). The phase assemblage including portlandite, ettringite, and carboaluminates was monitored using in-situ confocal Raman microscopy (CRM) and X-ray diffraction (XRD), and the hydration kinetics were studied through isothermal calorimetry (IC). Results revealed accelerated hydration in LC^3-MC compared to LC^3-CC, attributed to enhanced filler effect, increased reactivity, and the earlier formation of reaction products such as C-S-H gel. The different characterisation techniques demonstrated the earlier formation of portlandite and ettringite in LC^3-MC, with significant differences in water distribution and composition patterns. Mechanical activation also led to more rapid and extensive formation of carboaluminates, improving early-age compressive strength. These findings highlight the potential of mechanically activated clay in LC^3 systems to enhance the sustainability and performance of cementitious materials by optimising clinker replacement strategies.

1. Introduction

Hydration of Portland cement (PC) has been extensively studied due to its crucial role in the strength development of cementitious materials. Understanding the hydration process of conventional PC is challenging, as multiple phases coexist within the clinker. In cementitious systems, anhydrous cement powder reacts with water through intricate dissolution/precipitation reactions to form solid hydrates, which are responsible for cement properties and for binding aggregates in concrete and mortars [1]. The clinker composition and sulphate content govern the hydration of PC, producing key hydrated phases, such as the main hydrate calcium silicate hydrate (C-S-H), portlandite (CH), ettringite (AFt), and AFm phases (a family of hydrated calcium aluminate), all of which contribute to the development of PC properties [2–4].

In blended cements, the incorporation of supplementary cementitious materials (SCMs) introduces additional variables into the hydration process, making it more complex. The addition of SCMs modifies both the chemical reactions and resulting hydrates, as well as the kinetics of hydration. Additionally, SCMs provide extra nucleation sites and increase the water-to-clinker ratio, further influencing the hydration of clinker phases [5]. Therefore, early hydration is particularly critical in blended cement, as reduced clinker content may impact the properties of cement at short curing times [6]. In this regard, in-situ characterisation techniques are increasingly recognised for evaluating early-age hydration.

Recently, ternary blended cements, such as limestone calcined clay cement (LC^3), have gained interest in the construction sector. LC^3 incorporates limestone and calcined clay as SCMs, which exhibit a synergistic reaction that allows LC^3 to achieve properties comparable to PC while substantially reducing clinker content and carbon footprint [7–9]. To enhance its pozzolanic activity, clay must be activated, typically through calcination, which induces dehydroxylation of clay minerals, resulting in an amorphous structure and increased reactivity [10]. More recently, mechanical (mechanochemical) activation has emerged as an alternative method for enhancing the reactivity of clays [11]. This process breaks the structure of clay minerals through high-energy milling, producing highly amorphous materials with improved pozzolanic activity [12]. The effect of mechanical activation on clay structure

* Corresponding author.
E-mail address: chimenos@ub.edu (J.M. Chimenos).

https://doi.org/10.1016/j.conbuildmat.2024.139469
Received 16 September 2024; Received in revised form 7 November 2024; Accepted 2 December 2024
Available online 4 December 2024

and morphology has been extensively evaluated, and its suitability as a clinker replacement in blended cement has been demonstrated [13].

The replacement of clinker with calcined clay and limestone in LC^3 alters its hydration kinetics and microstructure, introducing further complexities in the evaluation of LC^3 hydration [14]. The principal variations in cement hydrates include the migration of aluminium from calcined clay into C-S-H to form calcium aluminium silicate hydrate (C-A-S-H), as well as the synergic reaction between limestone and calcined clay to form carboaluminate phases (AFm) [15,16]. At early-ages, the addition of limestone and calcined clay has been shown to enhance the hydration of clinker phases [17]. Furthermore, calcined clay with high metakaolinite content consumes portlandite through pozzolanic reactions during the early curing stages [18]. A previous study by the authors suggested that the hydration kinetics of LC^3 accelerated when mechanically activated kaolin replaced metakaolin [19]. Building on this, the present study aims to precisely determine the impact of mechanically activated clay on the hydration process and kinetics of LC^3 through a combination of in-situ techniques, which will provide valuable insights into the alterations in early-age properties induced by the incorporation of mechanically activated clay.

First, we evaluate the key characteristics of raw, thermally activated, and mechanically activated kaolin that may influence cement hydration. Next, we conduct a comprehensive investigation using in-situ confocal Raman microscopy (CRM), isothermal calorimetry (IC), and X-ray diffraction (XRD) to elucidate the hydration mechanisms of emerging LC^3 systems containing mechanically or thermally activated clay. By analysing the structural and microstructural evolution at different curing stages, we aim to gain insights into the fundamental processes occurring when water interacts with the diverse phases in these cementitious materials. Finally, we correlate the hydration data with compressive strength measurements at 1, 2, and 3 days of curing.

2. Materials and methods

2.1. Clay activation

The raw kaolinitic clay (RC), supplied by Minerals i Derivats, S.A., was thermally activated at 800 ºC for 1 h with a heating rate of 5 ºC/min as in previous experiments and literature to obtain calcined kaolinitic clay (CC) [20]. Mechanically activated kaolinitic clay (MC) was obtained using a PM 100 planetary ball mill from RETSCH in 500 mL zirconia jars, with 10 mm zirconia balls as grinding media. The milling parameters were set to rotation speed of 350 rpm and a milling time of 90 minutes, maintaining a balls-to-clay mass ratio of 20, as established in previous work [11]. Notably, mechanical activation consumed less electrical energy per gram of activated clay than thermal activation, 17.63 Wh/g and 42.82 Wh/g, respectively. However, the energy consumption will vary at the laboratory scale depending on the amount of clay activated, and the values cannot be extrapolated to the industrial scale [21].

Table 1 compiles the chemical composition of the clays determined through X-ray fluorescence (XRF) using an Axios spectrometer from Malvern Panalytical. The major oxides were SiO_2 and Al_2O_3, mainly corresponding to kaolinite, with minor amounts of K_2O and Fe_2O_3 also detected. The amount of SiO_2 and Al_2O_3 in CC is higher due to the loss of hydroxyls during the thermal activation, resulting in a minimal loss on ignition (LOI), while the composition of MC remains comparable to RC.

Table 1
Raw and activated clay chemical composition (XRF).

wt%	RC	CC	MC
SiO_2	49.85	56.44	49.59
Al_2O_3	36.31	41.12	36.09
K_2O	0.69	0.79	0.69
Fe_2O_3	0.47	0.51	0.45
CaO	0.16	0.11	0.10
TiO_2	0.15	0.17	0.15
Na_2O	0.13	0.03	0.02
MgO	0.11	0.09	0.08
P_2O_5	0.08	0.08	0.07
LOI	12.03	0.67	12.90

2.2. Activated clays characterisation

The main characteristics of raw and activated clay were assessed to better determine the effect of each clay type on the ternary blended cement. The crystalline and amorphous phases were evaluated and semi-quantified through XRD and Rietveld refinement using TOPAS. The amorphous content was estimated through the crystallinity index by fitting the amorphous halo with two broad peaks in TOPAS software. A Bragg-Brentano PANalytical X'Pert PRO MPD alpha1 diffractometer was used with the following conditions: CuKα_1 radiation (λ = 1.5406 Å), focalising Ge (111) primary monochromator, step size of 0.026o, anti-scatter slit of 4º, Soller slit of 0.04 rad, and five repeated scans with a measuring time of 24 min per scan.

Thermogravimetry (TG) was also used to determine the presence of water and hydroxyls in the clay samples through an SDT Q600 (TA Instruments) in a synthetic air atmosphere (50 mL/min) and with a heating rate of 10 ºC/min up to 1200 ºC. Approximately 20 mg of sample were placed into 90 µL open alumina crucibles.

The particle characteristics were also evaluated through particle size distribution (PSD), Brunauer-Emmett-Teller (BET) specific surface area (SSA), and scanning electron microscopy (SEM). PSD was assessed through laser diffraction in a Beckman Coulter LSTM 13 320 instrument equipped with a universal liquid module by dispersing a small amount of sample in ethanol by sonication. Furthermore, the BET-SSA was measured employing a TriStar 3000 V6.04 A device operated at 77.3 K with nitrogen as an inert gas. Particle morphology was observed by SEM in an FEI Quanta 200 operated at a working distance of approximately 10 mm and an accelerating voltage of 20 kV.

Moreover, the pozzolanic activity of raw and activated kaolinitic clay was evaluated through the R^3 test [22]. A paste containing a KOH and K_2SO_4 liquid solution and a $Ca(OH)_2$, $CaCO_3$, and clay solid blend was prepared with a liquid-to-solid ratio of 1.2. The mixture was blended in a high-shear mixer at 1300 rpm for 2 min, following the ASTM standard specifications [23]. The paste was then placed inside an isothermal calorimeter (TAM Air, TA Instruments) and the heat release from the pozzolanic reactions was measured at 40 ºC for 7 days.

2.3. LC^3 raw materials

The clinker used in this study was supplied by the Spanish company Cementos Molins, S.A. The material was received with a particle size < 4 mm and was first crushed to < 1 mm in a RETSCH BB51 jaw crusher, then milled in an RS100 vibratory disc mill (RETSCH), and finally sieved to achieve a particle size finer than 80 µm. The limestone and gypsum, with purities exceeding 98.5 wt% and 99 wt%, respectively, were acquired from LABKEM (Labbox, Spain). Furthermore, a poly-carboxylate ether (PCE) provided by CHRYSO Spain was used as a superplasticiser (SP).

Table 2 compiles the chemical composition of clinker and crystalline phase analysis determined by XRF and XRD, respectively, measured with the same conditions stated in Sections 2.1 and 2.2. The clinker predominantly consisted of CaO and SiO_2, with some Al_2O_3 and Fe_2O_3, corresponding to the traditional clinker phases C_3S (76 wt%), C_4AF, C_2S, and C_3A, and some common impurities: lime (CaO) and periclase (MgO). Furthermore, the physical attributes of mean particle size (d_{50}) and specific surface area of the raw materials are summarized in Table 3.

2.4. LC^3 mixing procedure and mix design

A ternary blend LC^3-50 formulation was used for the paste

Table 2
Clinker chemical composition and crystalline phases.

Chemical composition		Crystalline phases	
	wt%		wt%
SiO_2	21.06	C_3S	75.6
Al_2O_3	4.94	C_4AF	10.5
K_2O	0.91	C_2S	7.5
Fe_2O_3	3.67	C_3A	5.3
CaO	66.19	Lime	0.6
TiO_2	0.26	Periclase	0.6
Na_2O	0.18		
MgO	1.56		
P_2O_5	0.08		
LOI	1.14		

Table 3
Raw materials mean particle size and specific surface area.

	Clinker	Limestone	Gypsum
d_{50} (μm)	7.58	2.04	21.29
BET SSA (m^2/g)	0.84	11.07	0.86

preparation. Table 4 details the mix design of the LC^3 samples in mass percentages. In this formulation, 50 wt% of the clinker was replaced by activated clay (30 wt%), calcium carbonate (15 wt%), and gypsum (5 wt %). The formulation LC^3-50, containing 30 % of activated clay, was chosen for its proven capacity to achieve properties comparable to those of PC while significantly reducing the carbon footprint [24]. The nomenclatures LC^3-CC and LC^3-MC were used for the LC^3 formulated with thermally activated and mechanically activated kaolinitic clay, respectively. Following the formulation from a previous study [19], the PCE percentage was adjusted to maintain a water-to-binder (w/b) ratio of 0.4 and achieve a similar paste flow, measured by the mini-slump test [25]. Water and PCE contents are expressed as mass percentages of the total 100 wt% solid blend.

The cement pastes were prepared employing a high-shear mixer. Initially, the solid blend was mixed for 2 minutes at a rotational speed of 1000 rpm with 80 % or 70 % of the total water for LC^3-CC and LC^3-MC, respectively. Subsequently, the remaining 20 % or 30 % of the water and PCE, were incorporated and mixed for 2.5 minutes at a speed of 1800 rpm. The variation in the percentages of water was used to achieve similar fluidity during mixing. The paste was then used for the different characterisation techniques.

2.5. Cement characterisation

2.5.1. Early-hydration assessment

The heat evolution of cement hydration was monitored through IC in a TAM Air calorimeter (TA Instruments). The paste was prepared with the same conditions described in Section 2.4. Then, 10 g of the paste were placed into a plastic ampoule and introduced in the calorimeter. The heat release was measured at 20 ºC for 7 days. A reference plastic ampoule with water was also prepared to avoid noise from external temperature deviation.

The evolution of crystalline phases with increasing curing time was evaluated through in-situ XRD. The pastes were prepared, mounted front-loaded on sample holders, and covered with Kapton film (7.5 μm thick) to avoid water evaporation and carbonation. The in-situ XRD measurements were conducted using a PANalytical X'Pert PRO MPD powder diffractometer in the range 7–55 º2θ, with Ni-filtered CuKα radiation (λ = 1.5418 Å), with a step size of 0.026º, and measuring time of 3 minutes and 20 seconds per scan. Both cement samples were charged simultaneously, resulting in a diffractogram per sample every 8 minutes. The samples were measured for approximately 3 days, obtaining 549 diffractograms each. The first diffractograms for LC^3-MC and LC^3-CC were obtained at 15 and 18 min from the start of the paste preparation, respectively.

The diffractograms presented an irregular background mainly due to the presence of the Kapton film and amorphous phases from activated clay, free water, and C-S-H, which also contribute to the background of the diffractogram with amorphous halos. Furthermore, the short measuring time limited the resolution of the diffractograms. Therefore, given the difficulty and the potential error in full profile adjustment through Rietveld refinement, a semi-quantification was performed by fitting the main peak of selected hydrated phases, following the methodology reported in previous works [26].

Peak fitting was performed using the TOPAS software with the fundamental parameter approach function, which subtracts the equipment contribution to the peak using a LaB_6 calibration pattern. The phases were semi-quantified at 30-minute intervals to monitor the evolution of hydrates. For ettringite, the most intense peak at 9.1 2θº was selected, for hemicarboaluminate, the peak at 10.8 2θº, and for portlandite, the second most intense reflection at approximately 18.0 2θº, as the most intense peak at around 34.0 2θº significantly overlapped with clinker phases.

In this study, CRM was employed for in-situ measurements. A 5 mW laser with a 532 nm green laser was utilized, along with a 100X oil objective lens (N.A. 1.25). The laser had a theoretical spot size of approximately 500 nm laterally and 700 nm vertically. Scanning was conducted over a 40 × 40 μm area, resulting in a Raman image with parameters of 50 × 50 pixels and an integration time of 1.2 s per pixel.

For Raman analysis of reaction kinetics, a specially designed glass slide with a depression (26 ×76 x 1–1.2 mm thick) was utilized, covered by a glass slip to prevent water loss through evaporation during the curing process. The study examined various time points (t = 0, 1, 2, 4, 8, 10, 12, 24, and 48 h) in the same region to monitor changes in anhydrous pastes and new phases formed after hydration. Each Raman image took 30 min to acquire, with the age time denoting the start time for each measurement. Data analysis involved the use of Witec Control Plus Software (Witec, Ulm, Germany). The CRM data underwent "cosmic rays remove" (CRR) and "background subtraction" (BSub).

A criterion to semi-quantify the area occupied by a compound or phase was set as follows: a phase was considered present in a pixel if the area under the most intense band of its spectrum was five times greater than the noise in that spectral region [27–29]. The images representing each analysed phase were generated by calculating the area under the most intense Raman bands. Spectra were not normalized, but to ensure comparability across different time sweeps, laser power was adjusted to 20 mW before each measurement, maintaining uniform conditions (power, integration time, size of swept area, and number of points per sweep).

2.5.2. Early age strength

For the early age compressive strength test measurement, 8 cubic samples of 2x2x2 cm were prepared for each formulation and age. The samples were cured at ambient temperature in a climatised room

Table 4
Mixture proportions of LC^3 containing CC and MC.

	Clinker (%)	CC (%)	MC (%)	Limestone (%)	Gypsum (%)	Water (%)	w/b	PCE (%)
LC^3-CC	50	30	0	15	5	40	0.4	0.90
LC^3-MC	50	0	30	15	5	40	0.4	0.55

(T = 21 ± 1 ºC) and high relative humidity by placing them inside a sealed bag with a recipient filled with water. Compressive strength was measured at 1, 2, and 3 days of curing using an Incotecnic MULTI-R1 testing machine equipped with a 20 kN load cell, according to the EN 196–1 standard with a loading rate of 240 kg/s.

3. Results and discussion

3.1. Activated clay characterisation

Key characteristics of raw kaolin and thermally and mechanically activated kaolin were evaluated to fully understand the effect of incorporating activated clay in ternary blended cement. Fig. 1a displays the X-ray diffractograms of clay before and after activation. The RC was mainly composed of kaolinite with quartz, illite, and K-feldspar as minor mineral phases. The primarily flat background suggested a high crystallinity of the sample. Thermal activation caused the amorphisation of kaolinite, as evidenced by the absence of the reflections associated with this crystalline phase and the presence of a halo corresponding to the amorphous phase, centred at approximately 25 2θº. However, thermal treatment did not lead to the amorphisation of quartz or K-feldspar, and illite peaks were still detected. In contrast, mechanical activation resulted in the amorphisation of both kaolinite and illite. Furthermore, highly energetic mechanical treatments can also induce partial amorphisation of K-feldspar and quartz [30,31].

Fig. 1b shows the thermogravimetry related to heating raw and activated clay up to 1000 ºC. The mass loss associated with the release of hydroxyls from the kaolinite structure was no longer detected in CC since the structural disruption during thermal activation was caused by dehydroxylation. In contrast, mechanical activation caused the detachment of hydroxyls from the structure but not their release. Therefore, the temperature required for the weakly bonded hydroxyls' elimination in MC was much lower than for kaolinite dehydroxylation in RC. Furthermore, previous studies confirmed that some hydroxyls react to form water molecules adsorbed onto the material [26].

Table 5 compiles the results of a semi-quantitative phase quantification. The amorphous content was estimated through the crystallinity index method, and the crystalline phase percentages were recalculated based on the estimated amorphous content. The results revealed a high kaolinite content in RC of approximately 82 wt%, which was amorphised with both thermal and mechanical activation, leading to amorphous contents of about 90 wt% in both activated clays, slightly higher in MC. The percentages of the minor mineral phases remained similar after thermal activation, with slightly less dehydroxylated illite due to dehydroxylation and probably partial amorphisation. In contrast, illite was completely amorphised in MC, while quartz and K-feldspar were still detected with comparable percentages to RC.

Table 5
Crystalline and amorphous phases estimation of raw and activated clays.

	RC (wt%)	CC (wt%)	MC (wt%)
Kaolinite	82.0	-	0.5
Quartz	5.7	8.3	6.4
Illite	5.3	-	-
K-feldspar	1.6	1.0	1.0
Dehydroxylated illite	-	1.7	-
Amorphous content	5.4	89.0	92.0

The clay activation processes also caused alterations in particle size and morphology, as revealed in the PSD curves and SEM micrographs compiled in Fig. 2, along with the SSA results. Thermal activation led to some particle agglomeration detected in the differential particle volume, while the mean particle size remained constant, and the SSA was slightly reduced. In contrast, mechanical activation resulted in a significant particle size reduction, although some agglomeration was also observed in the PSD curve, which is typical of highly energetic milling processes [12]. A trimodal PSD curve was obtained, with a large volume of very fine particles (<10 μm) with the maximum at around 2 μm, and some agglomerates centred at approximately 13 and 23 μm. The structure disruption and particle size reduction resulted in a slight increase in the SSA despite the partial agglomeration of small particles.

SEM micrographs revealed that the particles of CC were similar to those of RC. Metakaolinite (amorphous kaolinite) particles also displayed platy and stacked morphology, indicating that thermal activation had slight effect on the particle morphology or size despite the structural disruption of kaolinite resulting from dehydroxylation. On the other hand, mechanical activation caused a significant reduction in the particle size, while some agglomeration can be observed due to the formation of new bonds between particles [32]. Furthermore, the particle morphology was also significantly altered, obtaining rounded and fine particles.

Mechanical and thermal activation also resulted in different pozzolanic activity of the activated clay. Fig. 3 displays the R^3 test results as (a) total heat release and (b) heat flow normalised per gram of solid. The measurements were performed from 50 min to 7 days instead of 75 min, which is the initial measuring time stated by the American standard [23] and followed by the authors in previous work [19]. The heat release results demonstrate the limited reactivity of RC, whereas both mechanical and thermal activation significantly increased the total heat

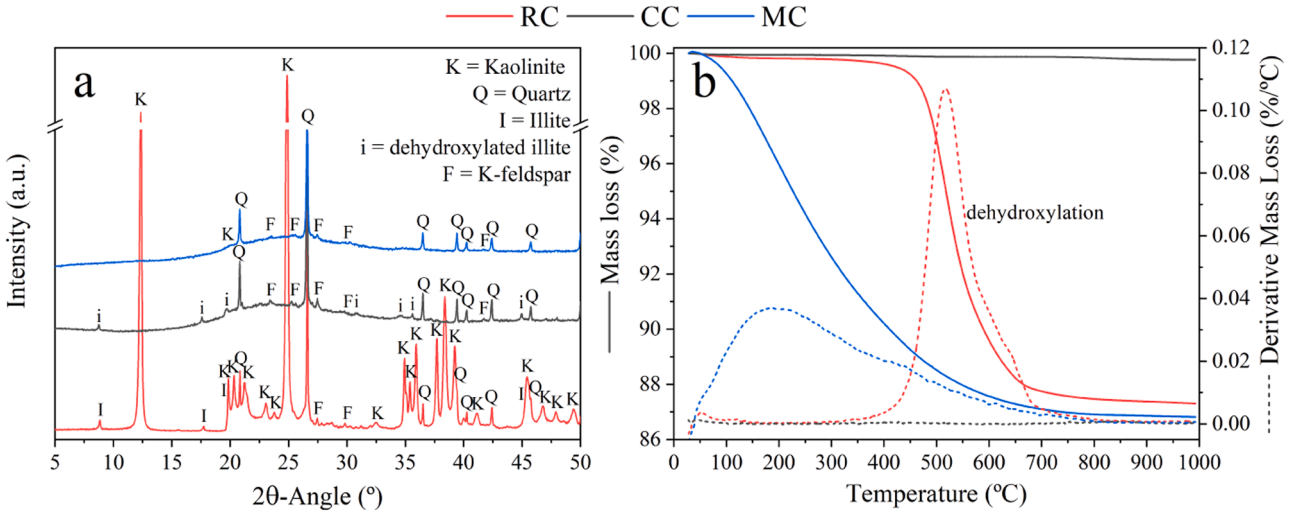

Fig. 1. (a) X-ray diffractograms and (b) thermogravimetry of RC, CC, and MC.

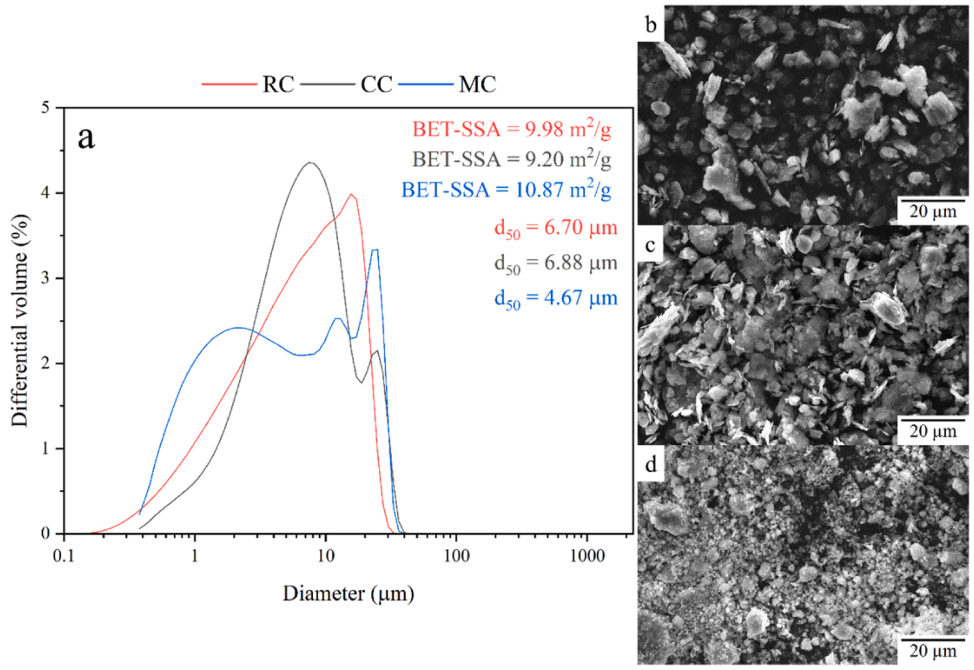

Fig. 2. (a) Particle size distribution of RC, CC, and MC and scanning electron micrographs of (b) RC, (c) CC, and (d) MC.

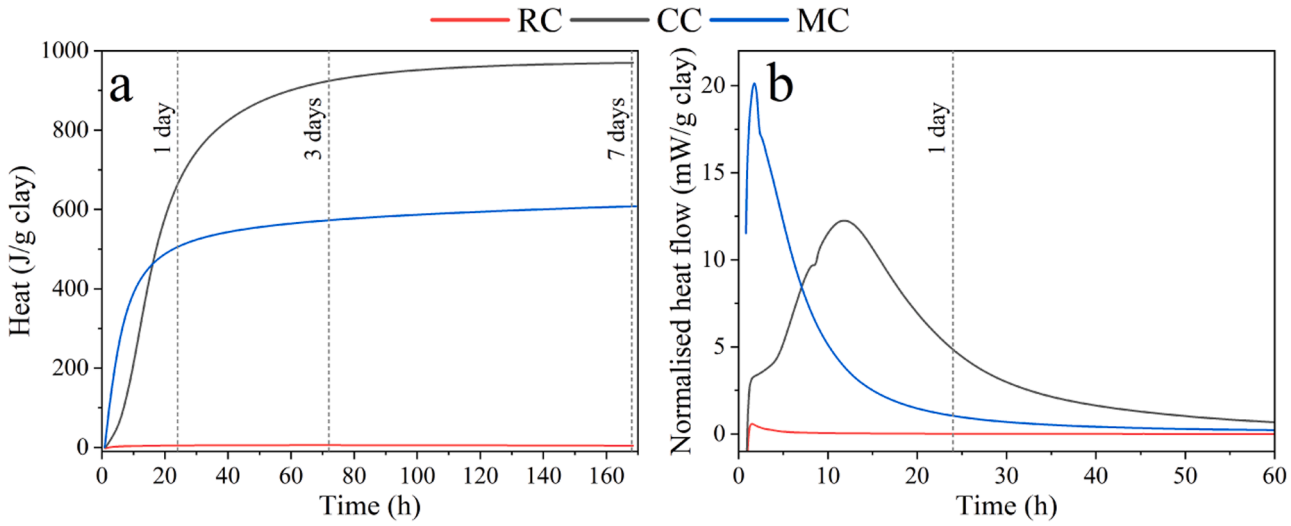

Fig. 3. Pozzolanic activity of RC, CC, and MC through R^3 test, (a) total heat release per gram of clay up to 7 days and (b) normalised heat flow per gram of clay up to 60 h.

release. The total heat release from CC was higher than from MC, partly caused by the presence of adsorbed water and weakly bonded hydroxyls in MC. However, MC's reaction rate is faster than CC's, potentially leading to the underestimation of the total heat release of MC, as reported with some SCMs that display accelerated pozzolanic reaction [33].

The faster pozzolanic reaction of MC was detected in the heat flow curves, where at 50 min, the heat flow of MC was already significantly high, suggesting that the reaction started well before this time. The heat flow curves display two main peaks; the first is assigned to ettringite formation, while the second corresponds to Al consumption to form carboaluminates [22]. Both peaks overlapped in the heat flow curves of CC and MC. MC's heat flow curve notably differed from CC's, exhibiting a very intense heat flow peak at very early times and finishing the main reaction peak much faster than CC's. The earlier reaction of MC is likely due to the smaller particle size compared to CC, which is commonly detected in mechanically activated clays [34]. Generally, the finer particle size expedites the formation of hydrated phases providing additional nucleation sites, and enables a faster dissolution of aluminate and silicate species [35]. Therefore, both ettringite and carboaluminate formation were detected earlier in MC.

Each activation method yields distinct clay characteristics that should affect their performance in ternary blended cement. Both CC and MC exhibit an amorphous structure rich in silica and alumina, but MC features additional water and weakly bonded hydroxyl groups. Mechanical activation also reduces clay particle size and changes its morphology and pore structure. Consequently, the behaviour of MC and CC in ternary blended cement is expected to differ significantly. The presence of free water in MC may contribute to reducing the water demand in blended cement, which is a known drawback of LC^3 [36]. Furthermore, the finer particles of MC could enhance the reactivity of the clay at early ages through enhanced filler effect, particularly

providing extra nucleation sites.

3.2. Cement hydration

3.2.1. Isothermal calorimetry

IC provides valuable information on the dissolution of clinker phases and the formation of new hydrated phases. The heat release steps of LC^3 have been extensively studied, with main peaks corresponding to C_3S hydration (S), aluminates reaction (A), and carboaluminates formation (AFm) [37]. The onset of the aluminate peak is related with anhydrous sulphate depletion in the system and a rapid formation of ettringite from sulphate ions desorbed from the C-S-H and aluminium, which produces a distinct peak in the heat flow signal [38].

The IC results of LC^3-CC and LC^3-MC, shown in Fig. 4, reveal similar reaction peaks in both samples, but with different reaction timings. Given that the same raw materials and water-to-cement ratio were used in LC^3-CC and LC^3-MC, the observed variations in cement hydration may be attributed to the addition of MC. LC^3-MC exhibited an earlier onset of the silicate peak and a higher maximum heat flow than LC^3-CC. This is commonly attributed to the filler effect of SCMs, which suggests that the filler effect of MC may be enhanced compared to that of CC, likely due to MC's finer particle size. This finer MC particles can provide additional nucleation points for C-S-H to grow [39]. In contrast, the platy particles of calcined clay tend to aggregate and stack, likely offering fewer reaction sites compared to the rounded particles of MC [40].

In addition, the earlier start of the aluminate peak (related to anhydrous sulphate depletion) in LC^3-MC suggests that MC promotes faster sulphate consumption and hydrated sulphate formation, primarily ettringite. Studies on mechanically activated clays suggest that MC's surface aluminium availability is enhanced due to lower binding energy, facilitating easier dissolution of aluminate groups, which could be the reason behind the faster reaction of sulphate and aluminates [13]. Furthermore, the filler effect also influences the time of anhydrous sulphate depletion, promoting higher C-S-H formation and consequently enhanced adsorption of sulphates by C-S-H [41]. Thus, the results suggest that MC exhibited a stronger filler effect compared to CC.

Moreover, the maximum heat flow of carboaluminates formation was also detected significantly earlier in LC^3-MC than in LC^3-CC, approximately 1 and 3 days, respectively. This supports the hypothesis that MC rapidly reacts in cement. The distinct characteristics of MC favour the early formation of C-(A)-S-H and carboaluminates through pozzolanic reactions.

Regarding total heat release, the faster reaction of LC^3 incorporating MC resulted in higher heat release at early ages, up to 3 days, whereas from 3 to 7 days, the heat release of LC^3-MC remained almost constant, as the main reactions had already taken place. In contrast, CC exhibited slower hydration, leading to higher heat release of LC^3-CC from around 80 h to 7 days. The rapid precipitation of hydration products in LC^3-MC, particularly carboaluminates, may result in lower available space as carboaluminates and hydrates fill the pores after clinker hydration [42]. Therefore, this limited space may slow down the growth of hydrates after the third day of hydration, resulting also in a slowdown of heat release [43].

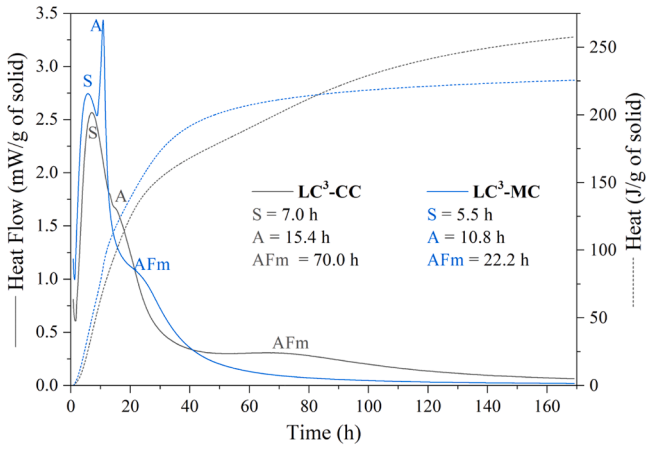

Fig. 4. Heat flow and heat measured through IC of LC^3-CC and LC^3-MC for up to 7 days.

3.2.2. In-situ X-ray diffraction

In-situ XRD is a robust methodology for investigating cement hydration at early ages as it provides continuous information on the reactions within the cement paste [44]. Fig. 5 displays diffractograms of LC^3-CC from 18 min to 73 h, divided into two regions: the 8–21 2θ° region for assessing the formation of hydrated products and gypsum depletion (Fig. 5a), and the 26–35 2θ° region to evaluate the consumption of anhydrous raw materials (Fig. 5b) over increasing curing time.

Initially, clinker phases reacted fast, detected by the decrease in C_3S reflections. As C_3S dissolved, reflections corresponding to portlandite (CH) progressively increased, reaching a maximum at around one day of curing, from where the rate of C_3S reaction appeared to decrease. The formation of C-S-H was not detected due to its amorphous nature, as the background humps are an overlap from amorphous clay, C-(A)-S-H, free water, and the Kapton film used to cover the samples [45]. Reflections associated with clinker's C_3A also decreased as aluminate species dissolved. Furthermore, from the early curing stages, gypsum reflections decreased as ettringite (Ett) formed through the reaction of sulphate ions from gypsum and aluminate species from C_3A or metakaolin. The development of ettringite, like CH formation, progresses gradually until reaching the maximum with anhydrous sulphate depletion. Calcite reflections exhibited limited reactivity within the first 72 h, while quartz remained unaffected due to its inherently low reactivity in cementitious systems. Intensity alterations in CH reflections are minor after reaching the maximum, indicating limited pozzolanic activity of CC during the initial curing period. Hemicarboaluminate (Hc) reflections were detected with very low intensities.

Fig. 6 displays the diffractograms of LC^3-MC from 15 min to 73 h in the same regions: the 8–21 2θ° range (Fig. 6a) and the 26–35 2θ° range (Fig. 6b), showing the progression of hydration with increasing curing time. Incorporating MC as a replacement for CC did not significantly alter the hydration products within the cement matrix. However, as evidenced by IC, the kinetics of hydration were notably accelerated.

During the initial curing stages, C_3S appeared to dissolve more rapidly in LC^3-MC than in LC^3-CC, leading to a quicker formation of CH and C-S-H, with an abrupt increase in the intensities of CH reflections. Consistent with IC results, the anhydrous sulphate depletion was also detected earlier in LC^3-MC than in LC^3-CC. The reflections of gypsum rapidly decreased as ettringite reflections abruptly increased. Moreover, in LC^3-MC, CH started decreasing at very early curing times, resulting in CH reflections with lower intensity than in LC^3-CC. The accelerated CH consumption was due to a rapid formation of carboaluminates (Hc) starting before 20 h of curing, indicating higher pozzolanic activity of MC at early ages [42].

In addition to carboaluminates formation, the pozzolanic reactions of MC probably contribute to the formation of C-A-S-H, as aluminium from clay usually migrates into the C-S-H structure [16]. However, due to overlapping signals in the background, the corresponding increase in the amorphous halo could not be detected through in-situ XRD. The intensities of carboaluminate reflections appeared higher in LC^3-MC compared to LC^3-CC at all ages up to 72 h. Remarkably, carboaluminates formation commenced right after the maximum ettringite content was reached, as observed in other LC^3 systems elsewhere [40]. Overall, the addition of MC induced an acceleration of hydration kinetics, resulting in a faster reaction of the components in the ternary blended cement.

The diffractograms are also displayed as a heatmap in Fig. 7 to facilitate better interpretation, allowing to quickly compare the hydration of both ternary blended cements. The heatmaps of LC^3-CC and LC^3-

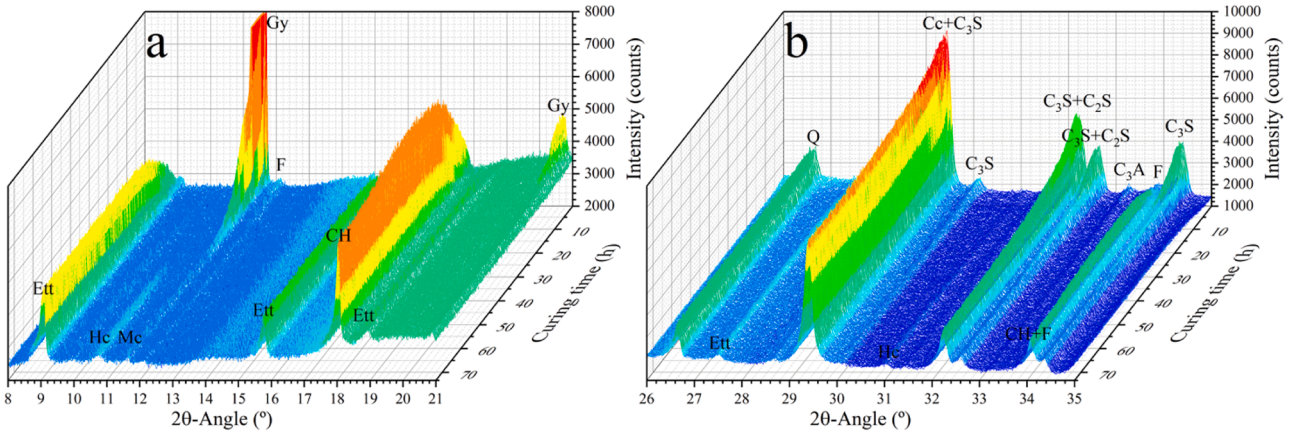

Fig. 5. In-situ XRD measurements of LC^3-CC up to 3 days from (a) 8–21 2θº and (b) 26–35 2θº. Ett: Ettringite; Hc: Hemicarboaluminate; Mc: Monocarboaluminate; Gy: Gypsum; F: Ferrite; CH: Portlandite; Q: Quartz; Cc: Calcite; C_3S: Alite; C_2S: Belite; C_3A: Aluminate.

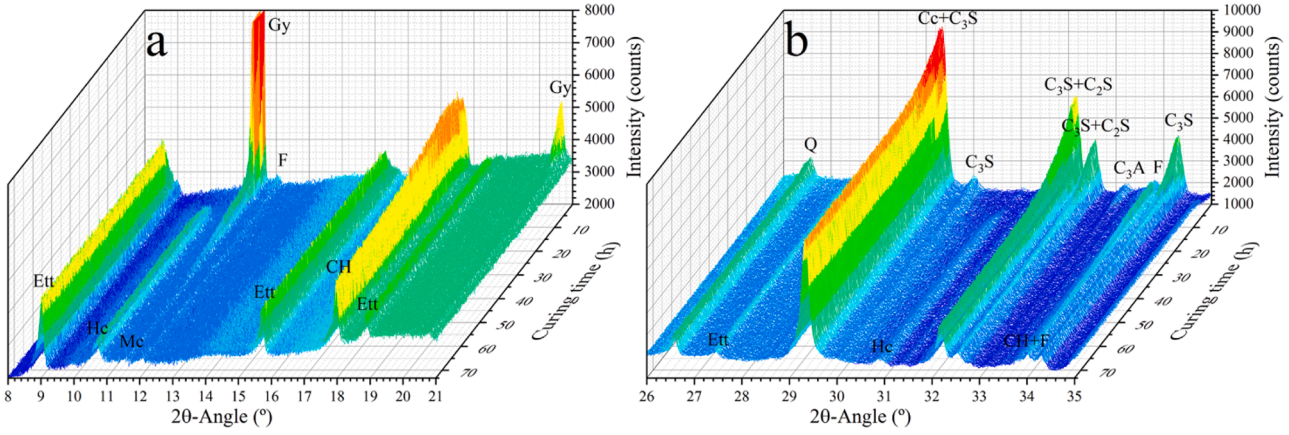

Fig. 6. In-situ XRD measurements of LC^3-MC up to 3 days from (a) 8–21 2θº and (b) 26–35 2θº. Ett: Ettringite; Hc: Hemicarboaluminate; Mc: Monocarboaluminate; Gy: Gypsum; F: Ferrite; CH: Portlandite; Q: Quartz; Cc: Calcite; C_3S: Alite; C_2S: Belite; C_3A: Aluminate.

MC provide a 2D representation, with the intensities in the diffractograms specified by a colour scale that ranges from purple (lowest intensity) to red (highest intensity), which is maintained for both systems to enhance the comprehensiveness of the comparison.

The accelerated reaction kinetics of LC^3-MC were readily distinguishable. As can be observed in Fig. 7, CH precipitated faster with the incorporation of MC, beginning at about 2 h in LC^3-MC compared to around 3 h in LC^3-CC, confirming the faster hydration of C_3S also detected in IC. Similarly, gypsum consumption was also accelerated, leading to the earlier detection of the maximum intensity of ettringite peaks at approximately 8 h in LC^3-MC and 20 h in LC^3-CC. This acceleration suggests that the aluminate reaction was also enhanced at early curing stages. Almost complete gypsum consumption was detected at the time of maximum ettringite content. However, a small amount of unreacted gypsum may have remained for up to 3 days in both blended cements. The position of the primary reflection of gypsum (~11.7 2θº) is very similar to that of monocarboaluminate, suggesting that the latter could contribute to the peak intensity. However, this is unlikely as monocarboaluminate is typically detected at later ages in LC^3 [46].

The amount of CH in LC^3-CC was significantly higher than in LC^3-MC at almost all curing times after CH precipitation started. The consumption of CH commenced much earlier in LC^3-MC due to the faster kinetics of pozzolanic reactions of MC. Consequently, portlandite was being consumed as it precipitated in LC^3-MC. This difference in reaction can be observed in the colour of CH reflection at around 18 2θº, which is red in LC^3-CC (highly intense) and yellow in LC^3-MC (less intense), thereby suggesting a significantly lower content in LC^3-MC. Accordingly, the precipitation of Hc was also detected earlier in LC^3-MC compared to LC^3-CC at approximately 10 and 35 h, respectively. Furthermore, the main peak of Hc was almost indiscernible in LC^3-CC, observed as a blurred line in the figure, indicating the low formation of this phase during the first 73 h of curing.

3.2.3. *Confocal Raman microscopy*

Irrespective of the type of activation used, whether thermal or mechanical, Fig. 8 shows the Raman spectra corresponding to the primary initial components, including clinker phases (C_2S and C_3S), gypsum, water, and the principal hydration products (ettringite and portlandite, among others), at various reaction times. The Raman spectrum of C_3S typically exhibits the ν_1 Raman band at ca. ~839 cm^{-1}, a poorly resolved shoulder at ~890 cm^{-1}, and a weaker doublet at ca. ~520–550 cm^{-1} [27,28]. The Raman spectrum of C_2S shows a dominant Raman band at ca. ~860 cm^{-1} with weaker Raman bands at ca. ~900 and ~980 cm^{-1} [27,28]. Additionally, characteristic Raman bands indicative of sulphate presence are evident, featuring an intense and narrow Raman band at ca. ~1022 cm^{-1} [28].

As anticipated, at 0 h of reaction, the formation of new phases such as portlandite or ettringite does not occur. Furthermore, CRM reveals the presence of water, marked by an intense and broad band centred on ca. 3400 cm^{-1} [28]. Thus, the microstructural localisation of water is demonstrated for the first time, alongside the other phases, during the cement particle hydration reaction.

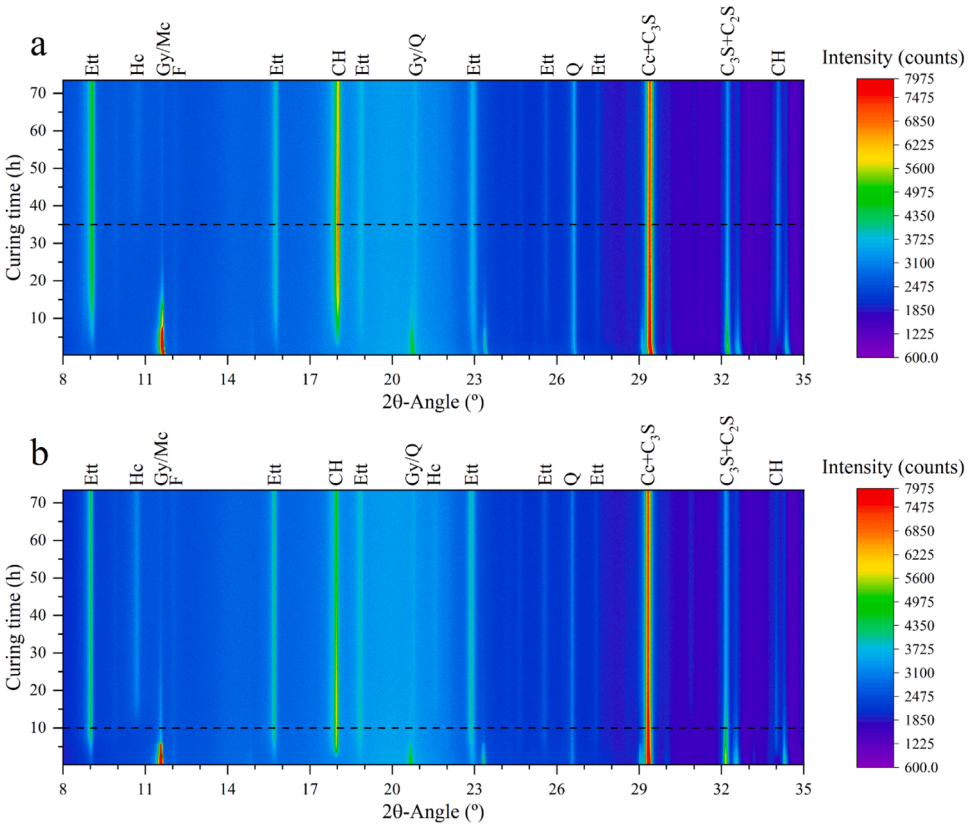

Fig. 7. In-situ XRD heatmap of (a) LC^3-CC and (b) LC^3-MC up to 3 days. Ett: Ettringite; Hc: Hemicarboaluminate; Mc: Monocarboaluminate; Gy: Gypsum; F: Ferrite; CH: Portlandite; Q: Quartz; Cc: Calcite; C_3S: Alite; C_2S: Belite. The dashed line represents the approximate start of Hc formation.

However, some differences can be observed between the two activation methods used using the CRM. One of the main differences is detected in the formation of CH. In Fig. 8b (LC^3-MC) the formation of CH can be seen in shorter times than in the LC^3-CC system. Specifically, after 2 h of reaction, slight nuclei of formed CH can be observed (see Fig. 9b). Nevertheless, regarding the formation of CH in the LC^3-CC system, it starts to become more evident around 4 h of reaction (see Fig. 9a). At reaction times of 4, 8, and 10 h (Fig. 8), the presence of CH becomes evident through the appearance of new Raman bands. A prominent and broad Raman band at ca. ~356 cm^{-1} is primarily attributed to OH transitions (ν_2Ca(OH)$_2$); the OH stretching band at ca. 3617 cm^{-1} (ν_1[Ca(OH)$_2$]) is characteristic of portlandite, along with weaker Raman bands at ca. 675 cm^{-1} due to OH rocking (ν_3[Ca(OH)$_2$]) [47].

Comparing average spectra (Fig. 8) and corresponding Raman mappings (Fig. 9), it is noted that the amount of reaction water decreases rapidly between 2 and 4 h, corresponding with the beginning of the acceleration period in IC due to the rapid formation of C-S-H and CH [48]. At 2 h, minimal CH is generated, but by 4 h, its formation becomes significant, peaking at 8 h and stabilizing thereafter. Fig. 9 illustrates how the presence of water decreases notably at 4, 8, and 10 h, while new regions of CH emerge, mainly attributed to C_3S hydration. Moreover, as the reaction time progresses (up to 48 h), the presence of CH becomes more evident and abundant in the LC^3-CC system. This corroborated that CH generated in the LC^3-MC system is produced faster but is also consumed earlier to the detriment of the formation of other secondary phases.

Between 12 and 24 h, the behaviour in both systems is very similar. A deceleration phase sets in Fig. 8 illustrates the average Raman spectra obtained during this hydration period, showing the continued presence of CH, C_2S, and C_3S phases, along with the disappearance of the Raman band corresponding to water. At this stage, unreacted water persists in the system, alongside a significant quantity of formed portlandite crystals. These crystals begin to impede the access of remaining water to C_3S and C_2S particles, despite their reduced size.

As time progresses, water consumption persists as portlandite crystals grow, resulting in a slower reaction between water and C_3S compared to the initial 12-h period. By the 48-h mark, the quantity of generated CH and the presence of water in the medium are nearly identical to those observed at 24 h. Additionally, the levels of C_2S and C_3S continue to diminish at a slower rate.

In addition, several key microstructural observations can be made from Fig. 9a and Fig. 9b: water fills most of the examined area in a connected manner. Although C_2S and C_3S are abundant in the Raman images from the beginning, there are differences in particle distribution. The C_2S and C_3S phases coexist (see Fig. 9) with slight changes between 0 and 2 h. As hydration progresses, the intensity of Raman bands at ca. ~839 cm^{-1} (C_3S) and at ca. 860 cm^{-1} (C_2S) decreases, indicating the ongoing reaction of both calcium silicates with water. In the LC^3-MC system, the presence of C_3S is given by the formation of agglomerates, which leads to a faster formation of the main reaction products, such as CH or C-S-H gel.

Moreover, at around 8 h, there is practically no C_3S remaining in the LC^3-MC system, while in LC^3-CC a certain amount is still present, indicating the accelerated reaction of this phase due to MC addition, which can be attributed to an enhanced filler effect. SCMs with very small particles, such as MC (see Fig. 2), provide extra nucleation space for hydrates to precipitate [49]. Despite the enhanced hydration, the apparent higher amount of water in LC^3-MC at all ages could be due to the presence of weakly bonded water and hydroxyls in MC, as shown in Fig. 1b, which is probably incorporated into the system. At 48 h, the amount of calcite in LC^3-CC remains almost constant, indicating its poor reactivity in the first 48 h of curing. In contrast, the area containing calcite in LC^3-MC is reduced with increasing curing time, indicating its reaction to form carboaluminates.

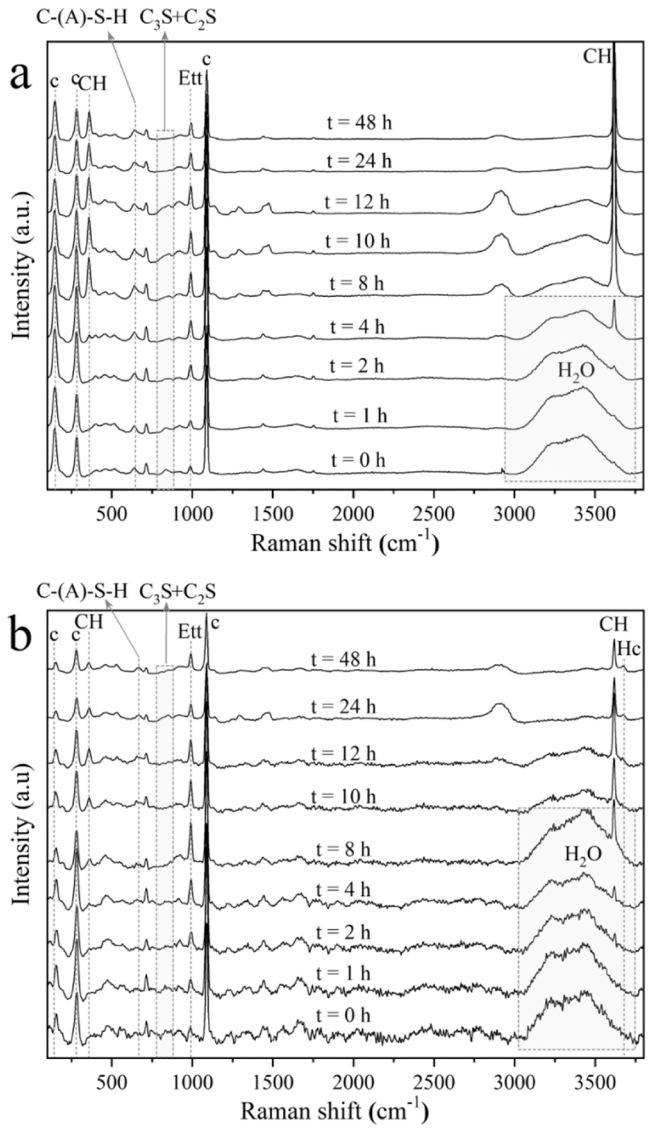

Fig. 8. Average Raman spectra of (a) LC^3-CC and (b) LC^3-MC at different hydration times obtained by CRM. Ett: Ettringite; c: carbonates; CH: portlandite; C_3S: Alite; C_2S: Belite; Hc: hemicarboaluminate.

As previously verified by conventional techniques such as XRD and IC, the formation of carboaluminate phases is also detected in Fig. 9 and Fig. 10 using CRM. Regarding the LC^3-CM system, the formation of this phase begins to be detected after 8 h of hydration, reaching a maximum formation at 12–24 h. A Raman band centred at around ca. 532 cm^{-1} corresponding to $Al(OH)_6$ is observed. The corresponding bands of the carbonate groups appear at wavenumbers at ca. 1088 cm^{-1}. This Raman band is attributed to the presence of weakly bound carbonate groups, which are located in the interlayer of the AFm phase between calcium alumino-ferrite layers [50]. Regarding the bands located at higher wavenumbers, the Raman spectra show a broad band centred at ca. 3682 cm^{-1}, with shoulders around at ca. 3631 cm^{-1} and 3560 cm^{-1}, which could be attributed to hydroxyls or water of the AFm phase.

However, the formation of Hc in the LC^3-CC system was not identified at short hydration times or even at older ages. The formation of the carboaluminate phase could only be detected by CRM in LC^3 incorporating mechanically activated clay. Factors such as particle size and the hydration processes of the rest of the majority phases may be affecting its formation as described previously. After the thermal activation process, a greater amount of CH is generated after 4 h of reaction. This CH formation could inhibit or slow down the formation of carboaluminates, making it very difficult to detect through CRM.

Fig. 11 compiles the CRM spectra and images corresponding to the formation of CH and sulphate hydrates. During the initial stage of hydration, an ettringite layer ($C_6As_3H_{32}$) forms on the surface of the C_3A particles, thus preventing the diffusion of SO_4^{2-}, OH^-, and Ca^{2+} ions [28,51,52]. The Raman band located at ca. 990 cm^{-1} corresponds to the presence of [SO_4^{2-}]. However, at short hydration times (0, 1, and 2 h) the formation of ettringite is limited, although there is evidence that it begins to start after 4 h of hydration (see Fig. 8). The sulphate hydrates were homogeneously distributed within the cement paste in both cement systems, and their content appeared to slightly decrease with increasing age.

The formation of ettringite becomes evident after 6–8 h of hydration, regardless of the clay activation process used (LC^3-CC or LC^3-MC). It is important to note that the formation of ettringite will depend on the availability of gypsum since it remains stable as long as there is enough gypsum in the medium [27,47,53]. In the average Raman spectra of Fig. 11a and Fig. 11c, there are hardly any differences, since the formation of ettringite occurs in both systems. However, as far as the distribution of ettringite along the studied area is concerned, slight differences can be appreciated as the reaction time evolves. The formation of ettringite is slightly lower after 10 h of hydration in the LC^3-MC system with respect to LC^3-CC as can be observed in the micrographs of Fig. 11d and Fig. 11b, respectively. This fact coincides with the formation of the phase corresponding to carboaluminates in the LC^3-MC system (Fig. 10b).

From 8 to 48 h, the content of CH was significantly higher in LC^3-CC compared to LC^3-MC due to the slower pozzolanic activity (see Fig. 11b and Fig. 11d). The images show that the CH regions remained virtually unaltered in LC^3-CC, whereas in LC^3-MC the regions were smaller at all ages and some reaction was detected, likely due to MC reaction to form Hc and other hydration products.

3.3. Semiquantitative phase assessment

The evolution of the crystalline hydrated phases in LC^3-CC and LC^3-MC with 30 min-intervals measured through XRD peaks areas is shown in Fig. 12. As aforementioned, the same hydrates precipitate in both LC^3 systems, starting with ettringite and followed by CH and Hc. However, significant differences in the kinetics and content of the hydrated phases are observed up to 3 days. Reflections of carboaluminates were first detected at 10 h and 36 h in LC^3-MC and LC^3-CC, respectively. The content of Hc rapidly increased in LC^3-MC from 10 to 20 h, after which it slowed down. In contrast, Hc slowly precipitated in LC^3-CC from 36 to 75 h without reaching contents similar to those of LC^3-MC, indicating slower pozzolanic reactions of CC compared to MC.

MC incorporation also led to an enhanced filler effect, detecting accelerated CH precipitation (2 h in LC^3-MC and 3 h in LC^3-CC) and higher CH content up to 10 h in LC^3-MC (see Fig. 12b). The faster precipitation of CH was likely accompanied by accelerated nucleation and growth of C-S-H from silicate and calcium ions in the liquid solution, as both hydrated phases form together during C_3S hydration after the induction period [1]. After 10 h, pozzolanic reactions started in LC^3-MC, and the CH content gradually began decreasing up to 75 h. In contrast, the CH content increased in LC^3-CC, indicating the low reactivity of CC in the first hours of curing up to approximately 25–30 h. From 30 h, the CH content remained constant until Hc began to precipitate at approximately 36 h, corresponding to the gradual decrease of CH content.

Ettringite was detected at all curing times for both systems, with its content increasing during early hydration and remaining constant for up to 3 days. The initial precipitation for up to 12 h is shown in Fig. 12c. Ettringite gradually increased, maintaining a similar reaction rate in both systems until approximately 5 h, when the ettringite content rapidly increased in LC^3-MC and reached the maximum at 8 h. The increase in the ettringite content is attributed to the renewed reaction of C_3A after gypsum depletion with sulphate ions adsorbed on the C-S-H gel

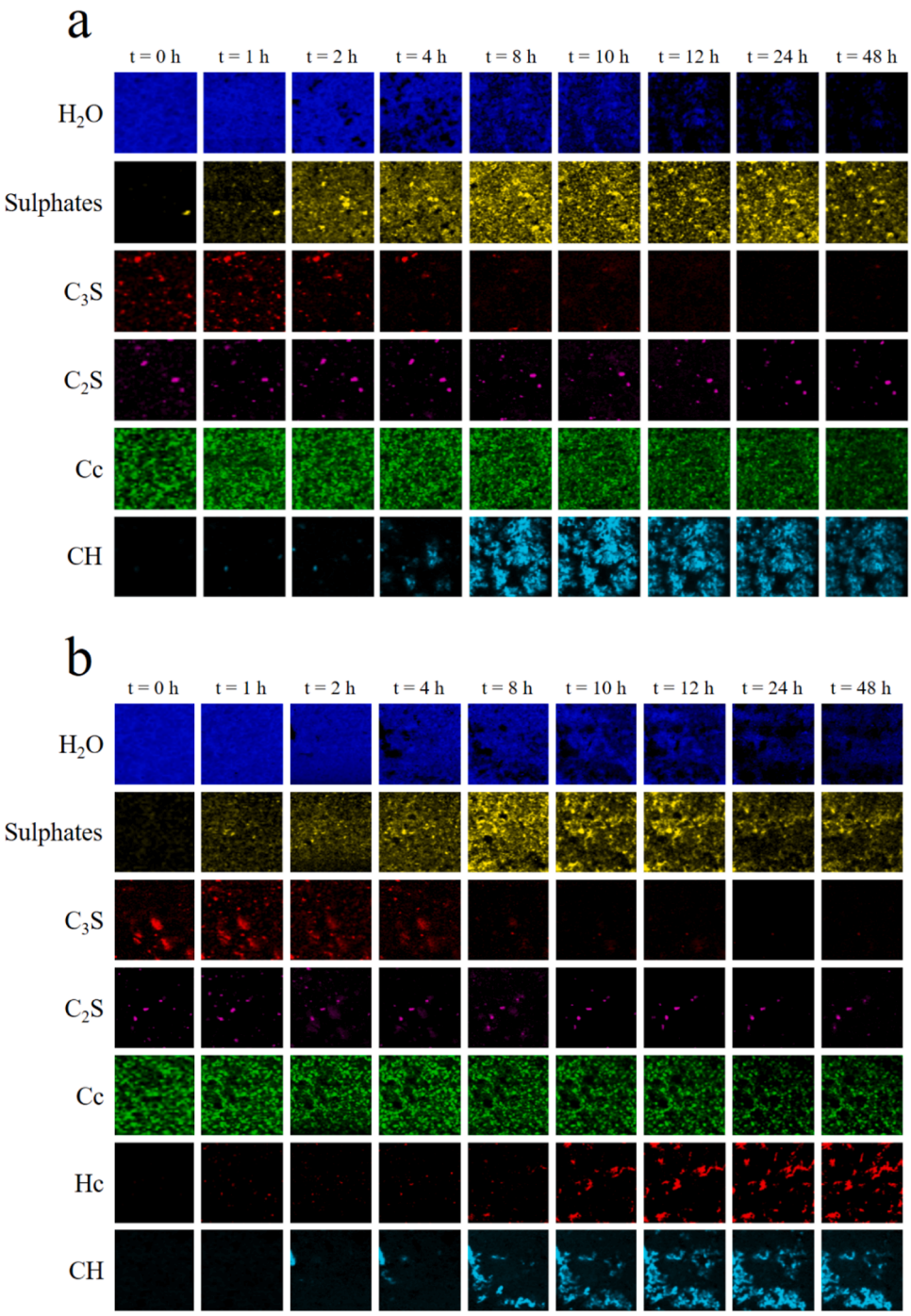

Fig. 9. Raman images by CRM of the evolution of the initial anhydrous phases and water: H_2O, C_3S (alite), C_2S (belite) and Cc (calcite), and the formation of new phases: Hc (hemicarboaluminate), sulphate hydrates, and CH (portlandite) at different hydration times for (a) system LC^3-CC and (b) system LC^3-MC.

[18]. In contrast, ettringite content gradually increased to 20–25 h due to slower gypsum depletion in LC^3-CC. Moreover, Hc precipitation only started after reaching the maximum of ettringite in LC^3-MC, which has been observed in LC^3 systems [41], suggesting that despite the accelerated hydration, Hc precipitation is probably prevented while ettringite is still forming.

The semiquantification of the hydrates was also performed by CRM for up to 48 h and is displayed in Fig. 13. A similar phase development was detected in CRM and XRD. After the earlier precipitation of CH (2 h) in LC^3-MC, its content increased to 12 h, when it began to decrease. Notably, with CRM, the CH content detected in LC^3-CC was higher than in LC^3-MC from 4 h, differing from XRD results, and it remained virtually constant from 8 to 48 h. The content of sulphate hydrates was higher in LC^3-MC due to faster precipitation up to 10 h, when it decreased and remained constant from 12 to 48 h. In LC^3-CC, the formation of sulphate hydrates was slower, but it reached a higher content at 10 h, slightly decreasing at later times. The formation of carboaluminates was first detected at 8–10 h in LC^3-MC, and it increased until 48 h, together with the decrease of CH. In contrast, Hc was not detected in LC^3-CC up to 48 h, which is the reason for the low reaction of CH. Therefore, the CRM results also verify the faster hydration of LC^3-MC, observing the enhanced filler effect of MC, causing the rapid formation of sulphate hydrates and CH, and the improved early pozzolanic activity, resulting in CH consumption and Hc precipitation.

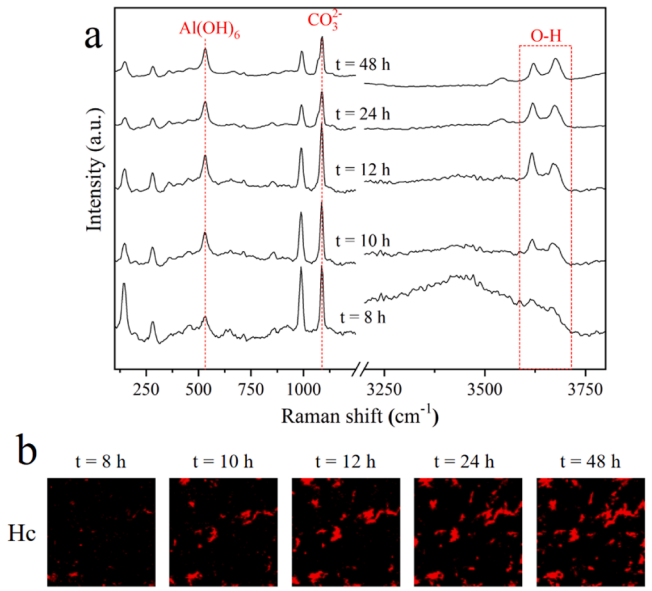

Fig. 10. Raman (a) spectra and (b) images following hemicarboaluminate (Hc) formation in LC^3-MC.

3.4. Early-age compressive strength

The in-situ techniques proved effective for evaluating the early hydration of LC^3, appropriately detecting the differences induced by the incorporation of MC replacing CC in the LC^3 system. The faster precipitation of hydrates in LC^3-MC should imply a more developed and compact microstructure, enhancing the properties of LC^3 at early curing times. The compressive strength was evaluated at 1, 2, and 3 days to determine the effect of enhanced early hydration on LC^3 performance (Fig. 14). C_3S is mainly responsible for early compressive strength, given its fast reaction kinetics to form C-S-H [54]. Therefore, the dilution effect caused by the 50 wt% of clinker reduction implies the lower presence of C_3S in the system, typically resulting in relatively low compressive strength at low curing times.

At 1 day, the compressive strength of LC^3-MC (22 MPa) was slightly higher than LC^3-CC (17 MPa). The enhanced filler effect before described should be responsible for the higher strength due to enhanced C-S-H formation. The early precipitation of Hc, beginning at approximately 10 h in LC^3-MC, could help increase the compressive strength at 1 day.

At 2 days, the effect of incorporating MC was notable, with a significant increase in compressive strength from 1 day (22 MPa) to 2 days (44 MPa). The strength of LC^3-MC almost doubled that of LC^3-CC (24 MPa), likely due to a more developed microstructure, with carboaluminates filling the porosity and improving the strength of the material [55]. The higher strength of LC^3-MC was still observed after 3 days, with measured compressive strengths of 54 MPa and 35 MPa for LC^3-MC and

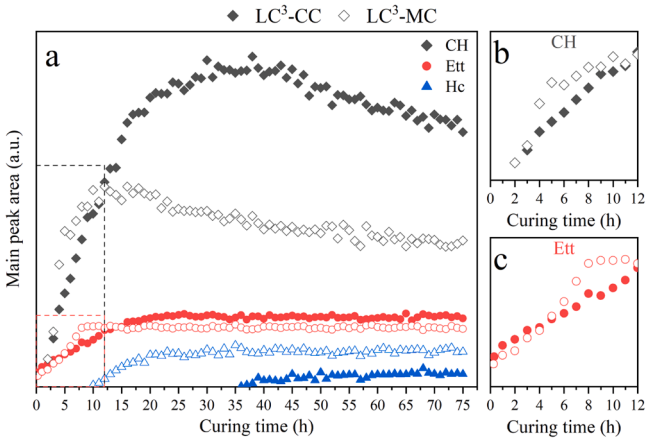

Fig. 12. XRD semiquantification of hydrated crystalline phases (a) portlandite (CH), ettringite (Ett), and hemicarboaluminate (Hc) for up to 75 h, (b) CH for up to 12 h, and (c) Ett for up to 12 h.

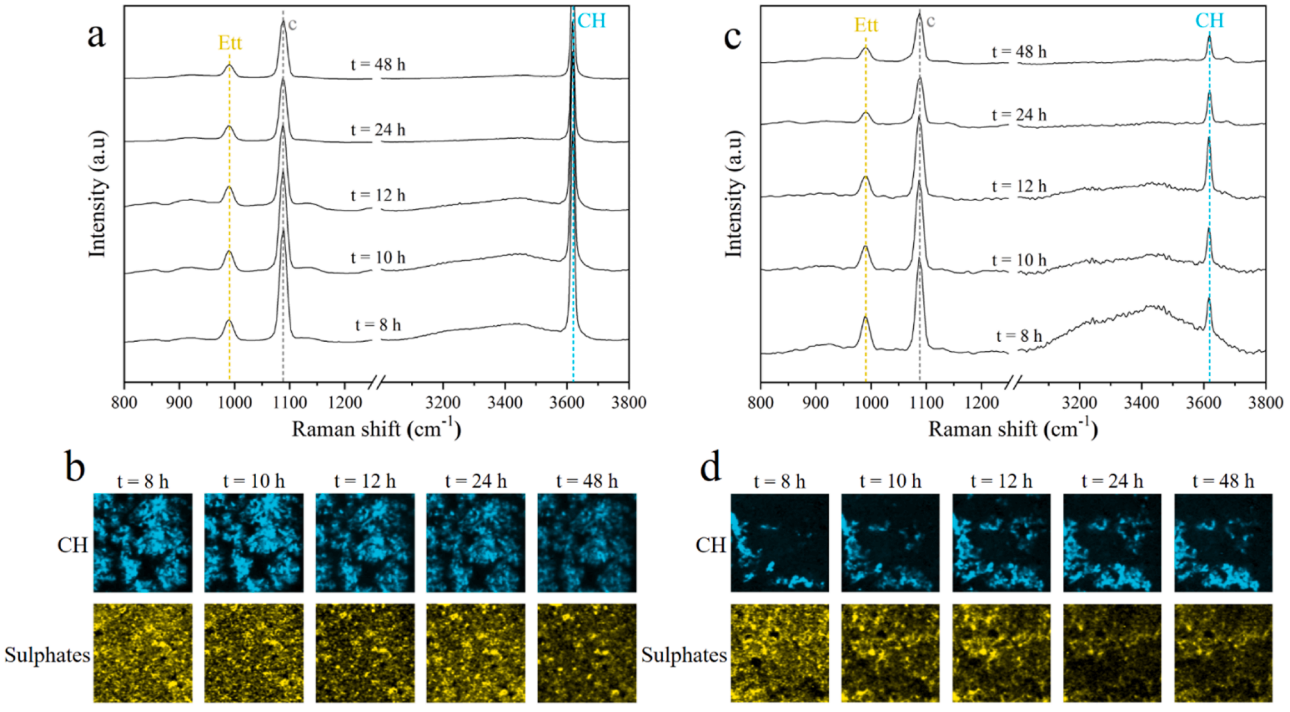

Fig. 11. Raman (a, c) spectra and (b, d) images for (a, b) LC^3-CC and (c, d) LC^3-MC following CH and sulphate hydrates formation from 8 to 48 h. Ett: Ettringite; c: carbonates; CH: portlandite.

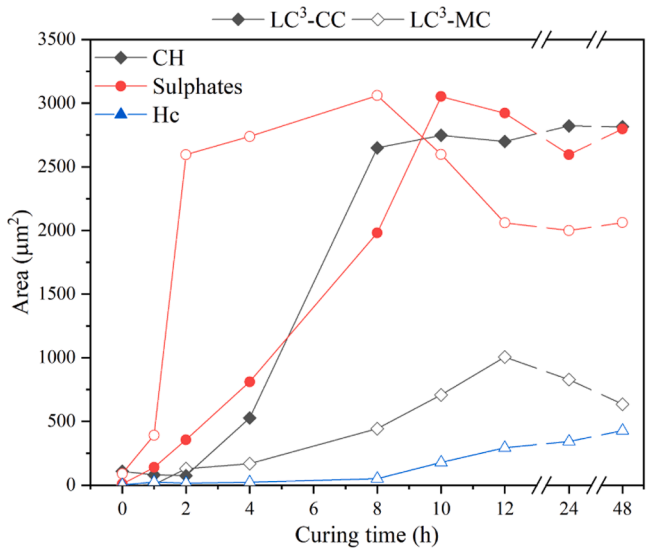

Fig. 13. CRM semiquantification of hydrated phases (CH, sulphate hydrates, and Hc) for up to 48 h.

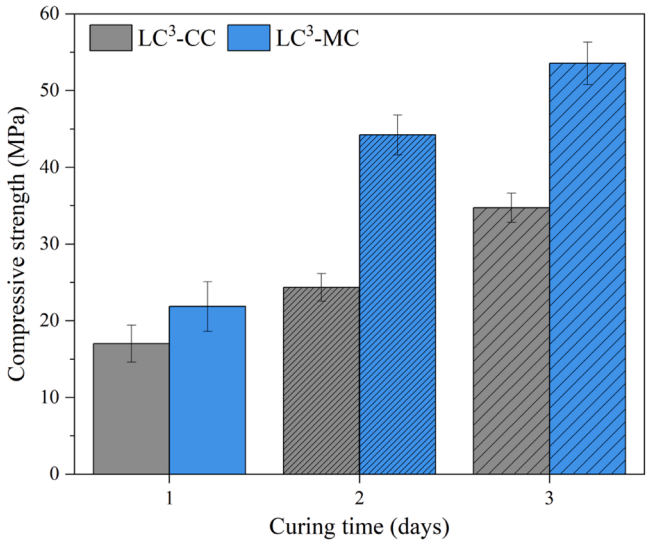

Fig. 14. Compressive strength of LC^3-CC and LC^3-MC at 1, 2, and 3 days of curing.

LC^3-CC, respectively. The strength of LC^3-CC increased notably, probably due to the development of pozzolanic reactions and the formation of a more compact microstructure.

Overall, the enhanced early hydration of LC^3-MC observed in previous characterisation techniques led to higher mechanical properties because of the accelerated precipitation of hydrates and microstructure evolution. The filler effect that caused faster C-S-H formation, likely contributed to microstructure development at 1 day, while the faster pozzolanic reactions likely contributed to porosity filling and enhanced packing, leading to higher compressive strength after 2 and 3 days of curing. The improved early strength confirms the superiority of MC in improving the early age performance of LC^3 blends.

4. Conclusions

This study investigated and compared the effect of thermal and mechanical clay activation methods on the early hydration of a low-carbon cement containing a high percentage of activated clay. Specifically, the evaluation focused on limestone calcined clay cement (LC^3), where the entire amount of thermally activated clay (CC) (30 wt %) was replaced by mechanically activated clay (MC). The properties of MC and CC were assessed, and the LC^3 containing CC (LC^3-CC) or MC (LC^3-MC) were then formulated. The following main conclusions were obtained:

- Both activation methods resulted in the amorphisation of kaolinite structure, but MC retained weakly bonded hydroxyls and water as it did not undergo dehydroxylation. Additionally, the particle morphology of MC was significantly altered, resulting in small and rounded particles and some degree of agglomeration compared to the platy-stacked crystals of CC.
- LC^3-MC exhibited faster hydration kinetics, as evidenced by the early detection of silicate and aluminate peaks in isothermal calorimetry. The presence of finer MC particles likely provided additional nucleation sites for C-S-H formation.
- Significant differences in water distribution and consumption patterns were observed between the two systems through in-situ confocal Raman microscopy and X-ray diffraction. Earlier portlandite and ettringite formation and expedited precipitation of carboaluminates were detected in LC^3-MC, the latter beginning at approximately 8–10 h and potentially contributing to porosity filling and achieving a denser microstructure.
- The enhanced early hydration in LC^3-MC resulted in superior early-age properties. By two days, LC^3-MC nearly doubled the strength of LC^3-CC, with this trend continuing at three days, confirming the positive impact of MC on early strength.

Overall, this study underscores the advantages of mechanical activation in promoting rapid and effective hydration in LC^3 systems. The findings highlight the potential of LC^3 systems containing MC to improve the sustainability and performance of cementitious materials, particularly at early ages by enhancing early hydration and strength development, which can partially offset the detrimental effects of reduced clinker content on hardened properties.

Future research should be focused on assessing the degree of reaction of activated clays and evaluating the effect of MC incorporation on the composition of C-(A)-S-H. Furthermore, an evaluation of the effect of MC and CC in the microstructure and porosity could further enhance the understanding of the impact of MC in the early curing of cement.

Funding

This work is partially supported by the Spanish Government with the Grants PID2021-125810OB-C21, PID2021-125810OB-C22, TED2021-129718B-I00, and TED2021-130633B-I00 funded by MCIN/AEI/10.13039/501100011033, by "ERDF A way of making Europe", and by the "European Union NextGenerationEU/PRTR" and the Catalan Government with the Grant 2021 SGR 00708. Furthermore, the Agència de Gestió d'Ajuts Universitaris i de Recerca (AGAUR) contributed through Mr. Jofre Mañosa's PhD grant (FI 2020).

CRediT authorship contribution statement

Jofre Mañosa: Writing – review & editing, Writing – original draft, Visualization, Resources, Methodology, Investigation, Formal analysis, Data curation, Conceptualization. **Manuel Torres-Carrasco:** Writing – review & editing, Writing – original draft, Visualization, Methodology, Investigation, Formal analysis. **Javier C. Córdoba:** Methodology, Investigation. **Alex Maldonado-Alameda:** Writing – review & editing, Visualization, Supervision. **Josep Maria Chimenos:** Writing – review & editing, Visualization, Supervision, Project administration, Funding acquisition, Conceptualization.

Declaration of Competing Interest

The authors declare that they have no known competing financial interests or personal relationships that could have appeared to influence the work reported in this paper.

Acknowledgements

The authors would like to thank the Catalan Government for the quality accreditation given to their research group DIOPMA (2021 SGR 00708). DIOPMA is a certified agent TECNIO in the category of technology developers from the Government of Catalonia. The authors are grateful to the companies Minerals i Derivats, S.A. and COM-CAL for the supply of the raw clay, to Cementos Molins S.A. for providing the clinker, and to CHRYSO Spain for supplying the superplasticizer. Furthermore, the authors show gratitude to the Scientific and Technological Centers of the Universitat de Barcelona (CCiTUB) for the XRD measurements. Mr. Jofre Mañosa is grateful to the Catalan Government for his research Grant, FI-DGR 2020. The authors acknowledge the support of CYTED Network ECoEICo—Circular Economy as a Strategy for a More Sustainable Construction Industry and the COST Action CircularB—Implementation of Circular Economy in the Built Environment.

Data Availability

Data will be made available on request.

References

[1] K.L. Scrivener, T. Matschei, F. Georget, P. Juilland, A.K. Mohamed, Advances in hydration and thermodynamics of cementitious systems, Cem. Concr. Res 174 (2023), https://doi.org/10.1016/j.cemconres.2023.107332.
[2] F. Zunino, K. Scrivener, The influence of sulfate addition on hydration kinetics and C-S-H morphology of C_3S and C_3S/C_3A systems, Cem. Concr. Res 160 (2022), https://doi.org/10.1016/j.cemconres.2022.106930.
[3] B. Lothenbach, F. Winnefeld, Thermodynamic modelling of the hydration of Portland cement, Cem. Concr. Res 36 (2006) 209–226, https://doi.org/10.1016/j.cemconres.2005.03.001.
[4] T. Matschei, B. Lothenbach, F.P. Glasser, The AFm phase in Portland cement, Cem. Concr. Res 37 (2007) 118–130, https://doi.org/10.1016/j.cemconres.2006.10.010.
[5] K.L. Scrivener, B. Lothenbach, N. De Belie, E. Gruyaert, J. Skibsted, R. Snellings, A. Vollpracht, TC 238-SCM: hydration and microstructure of concrete with SCMs: state of the art on methods to determine degree of reaction of SCMs, Mater. Struct. /Mater. Et. Constr. 48 (2015) 835–862, https://doi.org/10.1617/s11527-015-0527-4.
[6] A. Cuesta, A. Morales-Cantero, A.G. De la Torre, M.A.G. Aranda, Recent advances in C-S-H nucleation seeding for improving cement performances, Materials 16 (2023), https://doi.org/10.3390/ma16041462.
[7] B. Kanagaraj, N. Anand, R. Samuvel Raj, E. Lubloy, Techno-socio-economic aspects of Portland cement, geopolymer, and limestone calcined clay cement (LC^3) composite systems: a-state-of-art-review, Constr. Build. Mater. 398 (2023), https://doi.org/10.1016/j.conbuildmat.2023.132484.
[8] N. Ijaz, W.M. Ye, Z. ur Rehman, Z. Ijaz, M.F. Junaid, Global insights into micro-macro mechanisms and environmental implications of limestone calcined clay cement (LC3) for sustainable construction applications, Sci. Total Environ. 907 (2024), https://doi.org/10.1016/j.scitotenv.2023.167794.
[9] H. Wang, P. Hou, Q. Li, S. Adu-Amankwah, H. Chen, N. Xie, P. Zhao, Y. Huang, S. Wang, X. Cheng, Synergistic effects of supplementary cementitious materials in limestone and calcined clay-replaced slag cement, Constr. Build. Mater. 282 (2021), https://doi.org/10.1016/j.conbuildmat.2021.122648.
[10] A. Alujas Diaz, R.S. Almenares Reyes, T. Hanein, E.F. Irassar, M. Juenger, F. Kanavaris, M. Maier, A.T. Marsh, T. Sui, K.C. Thienel, L. Valentini, B. Wang, F. Zunino, R. Snellings, Properties and occurrence of clay resources for use as supplementary cementitious materials: a paper of RILEM TC 282-CCL, Mater. Struct. /Mater. Et. Constr. 55 (2022), https://doi.org/10.1617/s11527-022-01972-2.
[11] J. Mañosa, A.M. Gómez-Carrera, A. Svobodova-Sedlackova, A. Maldonado-Alameda, A. Fernández-Jiménez, J.M. Chimenos, Potential reactivity assessment of mechanically activated kaolin as alternative cement precursor, Appl. Clay Sci. 228 (2022), https://doi.org/10.1016/j.clay.2022.106648.
[12] I. Tole, K. Habermehl-Cwirzen, A. Cwirzen, Mechanochemical activation of natural clay minerals: an alternative to produce sustainable cementitious binders – review, Miner. Pet. 113 (2019) 449–462, https://doi.org/10.1007/s00710-019-00666-y.
[13] V.A. Baki, X. Ke, A. Heath, J. Calabria-Holley, C. Terzi, M. Sirin, The impact of mechanochemical activation on the physicochemical properties and pozzolanic reactivity of kaolinite, muscovite and montmorillonite, Cem. Concr. Res 162 (2022) 106962, https://doi.org/10.1016/j.cemconres.2022.106962.
[14] A.H. Ahmed, S. Nune, M. Liebscher, T. Köberle, A. Willomitzer, I. Noack, M. Butler, V. Mechtcherine, Exploring the role of dilutive effects on microstructural development and hydration kinetics of limestone calcined clay cement (LC^3) made of low-grade raw materials, J. Clean. Prod. 428 (2023), https://doi.org/10.1016/j.jclepro.2023.139438.
[15] Y. Zhao, Y. Zhang, A review on hydration process and setting time of limestone calcined clay cement (LC3), Solids 4 (2023) 24–38, https://doi.org/10.3390/solids4010003.
[16] F. Avet, E. Boehm-Courjault, K. Scrivener, Investigation of C-A-S-H composition, morphology and density in Limestone Calcined Clay Cement (LC^3), Cem. Concr. Res 115 (2019) 70–79, https://doi.org/10.1016/j.cemconres.2018.10.011.
[17] F. Avet, K. Scrivener, Investigation of the calcined kaolinite content on the hydration of Limestone Calcined Clay Cement (LC^3), Cem. Concr. Res 107 (2018) 124–135, https://doi.org/10.1016/j.cemconres.2018.02.016.
[18] A. Morales-Cantero, A.G. De la Torre, A. Cuesta, I. Santacruz, I.M.R. Bernal, O. Mazanec, A. Dalla-Libera, P. Borralleras, M.A.G. Aranda, In situ synchrotron powder diffraction study of LC^3 cement activation at very early ages by C-S-H nucleation seeding, Cem. Concr. Res 178 (2024), https://doi.org/10.1016/j.cemconres.2024.107463.
[19] J. Mañosa, S. Huete-Hernández, A. Alvarez-Coscojuela, A. Maldonado-Alameda, J. M. Chimenos, Comparative study of limestone calcined clay cement produced with mechanically activated kaolin and calcined kaolin, J. Build. Eng. 97 (2024) 110748, https://doi.org/10.1016/j.jobe.2024.110748.
[20] F. Zunino, K. Scrivener, Reactivity of kaolinitic clays calcined in the 650 °C–1050 °C temperature range: towards a robust assessment of overcalcination, Cem. Concr. Compos 146 (2024) 105380, https://doi.org/10.1016/j.cemconcomp.2023.105380.
[21] J. Mañosa, A. Alvarez-Coscojuela, A. Maldonado-Alameda, J.M. Chimenos, A lab-scale evaluation of parameters influencing the mechanical activation of kaolin using the design of experiments, Materials 17 (2024), https://doi.org/10.3390/ma17184651.
[22] F. Avet, R. Snellings, A. Alujas Diaz, M. Ben Haha, K. Scrivener, Development of a new rapid, relevant and reliable (R^3) test method to evaluate the pozzolanic reactivity of calcined kaolinitic clays, Cem. Concr. Res 85 (2016) 1–11, https://doi.org/10.1016/j.cemconres.2016.02.015.
[23] ASTM International, C 1897-20 "Standard Test Methods for Measuring the Reactivity of Supplementary Cementitious Materials by Isothermal Calorimetry and Bound Water Measurements," West Conshohocken, PA, 2020. https://doi.org/10.1520/C1897-20.2.
[24] M. Sharma, S. Bishnoi, F. Martirena, K. Scrivener, Limestone calcined clay cement and concrete: a state-of-the-art review, Cem. Concr. Res 149 (2021) 106564, https://doi.org/10.1016/j.cemconres.2021.106564.
[25] Z. Tan, S.A. Bernal, J.L. Provis, Reproducible mini-slump test procedure for measuring the yield stress of cementitious pastes, Mater. Struct. /Mater. Et. Constr. 50 (2017) 1–12, https://doi.org/10.1617/s11527-017-1103-x.
[26] J. Mañosa, J.Calvo-de la Rosa, A. Silvello, A. Maldonado-Alameda, J.M. Chimenos, Kaolinite structural modifications induced by mechanical activation, Appl. Clay Sci. 238 (2023), https://doi.org/10.1016/j.clay.2023.106918.
[27] M. Torres-Carrasco, A. del Campo, M.A. de la Rubia, E. Reyes, A. Moragues, J. F. Fernández, New insights in weathering analysis of anhydrous cements by using high spectral and spatial resolution Confocal Raman Microscopy, Cem. Concr. Res 100 (2017) 119–128, https://doi.org/10.1016/j.cemconres.2017.06.003.
[28] M. Torres-Carrasco, A. del Campo, M.A. de la Rubia, E. Reyes, A. Moragues, J. F. Fernández, In situ full view of the Portland cement hydration by confocal Raman microscopy, J. Raman Spectrosc. 50 (2019) 720–730, https://doi.org/10.1002/jrs.5574.
[29] T. Dieing, O. Hollricher, J. Toporski, Confocal Raman Microscopy, Springer, Berlin, 2010, https://doi.org/10.1007/978-3-642-12522-5.
[30] G. Yao, Z. Wang, J. Yao, X. Cong, C. Anning, X. Lyu, Pozzolanic activity and hydration properties of feldspar after mechanical activation, Powder Technol. 383 (2021) 167–174, https://doi.org/10.1016/j.powtec.2021.01.042.
[31] Q. Wan, Y. Zhang, R. Zhang, Using mechanical activation of quartz to enhance the compressive strength of metakaolin based geopolymers, Cem. Concr. Compos 111 (2020) 103635, https://doi.org/10.1016/j.cemconcomp.2020.103635.
[32] P. Baláž, Mechanochemistry in Nanoscience and Minerals Engineering, Springer, Berlin, 2008, https://doi.org/10.1007/978-3-540-74855-7.
[33] K. Weise, N. Ukrainczyk, E. Koenders, Early metakaolin reactions in pozzolanic R^3-test: calorimetry baseline correction of initial temperature jump due to ex-situ mixing, Mater. Struct. 56 (2023) 129, https://doi.org/10.1617/s11527-023-02217-6.
[34] J. Mañosa, A. Alvarez-Coscojuela, J. Marco-Gibert, A. Maldonado-Alameda, J. M. Chimenos, Enhancing reactivity in muscovitic clays: Mechanical activation as a sustainable alternative to thermal activation for cement production, Appl. Clay Sci. 250 (2024) 107266, https://doi.org/10.1016/j.clay.2024.107266.
[35] D. Ndahirwa, H. Zmamou, H. Lenormand, N. Leblanc, The role of supplementary cementitious materials in hydration, durability and shrinkage of cement-based materials, their environmental and economic benefits: a review, Clean. Mater. 5 (2022), https://doi.org/10.1016/j.clema.2022.100123.
[36] L. Lei, M. Palacios, J. Plank, A.A. Jeknavorian, Interaction between polycarboxylate superplasticizers and non-calcined clays and calcined clays: a review, Cem. Concr. Res 154 (2022) 106717, https://doi.org/10.1016/j.cemconres.2022.106717.
[37] L.G. Py, J.S.A. Neto, M.A. Longhi, A.P. Kirchheim, Evaluation of ultrafine calcined clays on LC^3 cements on the sulfate requirement, water demand and strength

development, Mater. Struct. /Mater. Et. Constr. 57 (2024), https://doi.org/10.1617/s11527-023-02288-5.
[38] M.R.C. da Silva, J. da, S. Andrade Neto, B. Walkley, A.P. Kirchheim, Exploring sulfate optimization techniques in Limestone Calcined Clay Cements (LC^3): limitations and insights, Cem. Concr. Res 175 (2024), https://doi.org/10.1016/j.cemconres.2023.107375.
[39] T. Oey, A. Kumar, J.W. Bullard, N. Neithalath, G. Sant, The filler effect: the influence of filler content and surface area on cementitious reaction rates, J. Am. Ceram. Soc. 96 (2013) 1978–1990, https://doi.org/10.1111/jace.12264.
[40] M. Maier, R. Sposito, N. Beuntner, K.C. Thienel, Particle characteristics of calcined clays and limestone and their impact on early hydration and sulfate demand of blended cement, Cem. Concr. Res 154 (2022), https://doi.org/10.1016/j.cemconres.2022.106736.
[41] F. Zunino, K. Scrivener, The influence of the filler effect on the sulfate requirement of blended cements, Cem. Concr. Res 126 (2019), https://doi.org/10.1016/j.cemconres.2019.105918.
[42] F. Zunino, K. Scrivener, The reaction between metakaolin and limestone and its effect in porosity refinement and mechanical properties, Cem. Concr. Res 140 (2021), https://doi.org/10.1016/j.cemconres.2020.106307.
[43] Y. Briki, F. Avet, M. Zajac, P. Bowen, M.Ben Haha, K. Scrivener, Understanding of the factors slowing down metakaolin reaction in limestone calcined clay cement (LC^3) at late ages, Cem. Concr. Res 146 (2021), https://doi.org/10.1016/j.cemconres.2021.106477.
[44] P.R. de Matos, J.S. Andrade Neto, D. Jansen, A.G. De la Torre, A.P. Kirchheim, C.E. M. Campos, In-situ laboratory X-ray diffraction applied to assess cement hydration, Cem. Concr. Res 162 (2022), https://doi.org/10.1016/j.cemconres.2022.106988.
[45] S.T. Bergold, F. Goetz-Neunhoeffer, J. Neubauer, Quantitative analysis of C-S-H in hydrating alite pastes by in-situ XRD, Cem. Concr. Res 53 (2013) 119–126, https://doi.org/10.1016/j.cemconres.2013.06.001.
[46] R. Hay, K. Celik, Performance enhancement and characterization of limestone calcined clay cement (LC^3) produced with low-reactivity kaolinitic clay, Constr. Build. Mater. 392 (2023), https://doi.org/10.1016/j.conbuildmat.2023.131831.
[47] C.-S. Deng, C. Breen, J. Yarwood, S. Habesch, J. Phipps, B. Craster, G. Maitland, Ageing of oilfield cement at high humidity: a combined FEG-ESEM and Raman microscopic investigation, J. Mater. Chem. 12 (2002) 3105–3112, https://doi.org/10.1039/b203127m.
[48] K. Scrivener, A. Ouzia, P. Juilland, A. Kunhi Mohamed, Advances in understanding cement hydration mechanisms, Cem. Concr. Res 124 (2019), https://doi.org/10.1016/j.cemconres.2019.105823.
[49] E. Berodier, K. Scrivener, Understanding the filler effect on the nucleation and growth of C-S-H, J. Am. Ceram. Soc. 97 (2014) 3764–3773, https://doi.org/10.1111/jace.13177.
[50] L.G. Baquerizo, T. Matschei, K.L. Scrivener, M. Saeidpour, L. Wadsö, Hydration states of AFm cement phases, Cem. Concr. Res 73 (2015) 143–157, https://doi.org/10.1016/j.cemconres.2015.02.011.
[51] S.C.B. Myneni, S.J. Traina, G.A. Waychunas, T.J. Logan, Vibrational spectroscopy of functional group chemistry and arsenate coordination in ettringite, Geochim Cosmochim. Acta 62 (1998) 3499–3514, https://doi.org/10.1016/S0016-7037(98)00221-X.
[52] J. Bensted, Uses of Raman spectroscopy in cement chemistry, J. Am. Ceram. Soc. 59 (1976) 140–143, https://doi.org/10.1111/j.1151-2916.1976.tb09451.x.
[53] L. Black, Raman spectroscopy of cementitious materials, in: Spectroscopic Properties of Inorganic and Organometallic Compounds, Royal Society of Chemistry, Cambridge, 2009, pp. 72–127, https://doi.org/10.1039/b715000h.
[54] A. Kumar, S. Bishnoi, K.L. Scrivener, Modelling early age hydration kinetics of alite, Cem. Concr. Res 42 (2012) 903–918, https://doi.org/10.1016/j.cemconres.2012.03.003.
[55] F. Zunino, K. Scrivener, Microstructural developments of limestone calcined clay cement (LC^3) pastes after long-term (3 years) hydration, Cem. Concr. Res 153 (2022), https://doi.org/10.1016/j.cemconres.2021.106693.